Mineralogical Magazine, February 2015, Vol. 79(1), pp. 71–87

Thermal expansion behaviour of orthopyroxenes: the role of the Fe-Mn substitution

L. Scandolo[1], M. L. Mazzucchelli[1], M. Alvaro[2,*,†], F. Nestola[2], F. Pandolfo[1] and M. C. Domeneghetti[1]

[1] Dipartimento di Scienze della Terra e dell'Ambiente, Università degli Studi di Pavia, Italy
[2] Dipartimento di Geoscienze, Università degli Studi di Padova, Italy

[*Received 30 March 2014; Accepted 6 July 2014; Associate Editor: W. Crichton*]

ABSTRACT

Two *Pbca* orthopyroxene samples, donpeacorite (DP N.1) and enstatite (B22 N.60) with chemical formulae $Mn_{0.54}Ca_{0.03}Mg_{1.43}Si_2O_6$ (X_{Mn} = 0.27) and $Fe_{0.54}Ca_{0.03}Mg_{1.43}Si_2O_6$ (X_{Fe} = 0.27), respectively, were investigated by single-crystal X-ray diffraction at high-temperature conditions.

The nearly identical X_{Fe} and X_{Mn} make the two samples the perfect candidates to investigate the effect of the compositional change at the *M*2 site (i.e. Fe-Mn substitution) on the thermal expansion behaviour of orthopyroxenes.

Therefore, the unit-cell parameter thermal expansion behaviour of both samples has been investigated in the temperature range between room *T* and 1073 K. No evidence for phase transitions was found over that range. The two samples have been previously disordered with an *ex situ* annealing at ~1273 K.

The unit-cell parameters and volume thermal expansion data, collected on the disordered samples, have been fitted to a Fei Equation of State (EoS) and the following coefficients obtained: V_0 = 853.35(4) Å^3, $\alpha_{V,303K} = 2.31(24) \times 10^{-5}$ K^{-1} and V_0 = 845.40(6) Å^3, $\alpha_{V,303K} = 2.51(25) \times 10^{-5}$ K^{-1} for DP N.1 and B22 N.60, respectively.

While there is no difference in the volume thermal expansion coefficient as a function of composition and the expansion along the **b** direction is nearly identical for both samples, slight differences have been found along **a** and **c** lattice directions. The thermal expansion along the **a** direction is counterbalanced by that along **c** being responsible for the changes in lattice expansion scheme from $\alpha_b > \alpha_c > \alpha_a$ at room *T*, to $\alpha_c > \alpha_b > \alpha_a$ at high *T*. Therefore, as a result of the different behaviour along **a** and **c**, the unit-cell volume thermal expansion for both samples is identical within estimated standard deviations. The negligible effect of the Fe-Mn substitution on the bulk thermal expansion can be applied when dealing with geothermobarometry based on the elastic host-inclusion approach (e.g. Nestola *et al*., 2011; Howell *et al*., 2010; Angel *et al*., 2014*a*,*b*, 2015). In fact, though the compressibility effect is still not known, the nearly identical thermal expansion coefficients will not affect the entrapment pressure (P_e).

Keywords: orthopyroxene, thermal expansion, single-crystal X-ray diffraction, order-disorder.

Introduction

Orthopyroxene (OPX) is a major component in the crust and in mineralogical models of the Earth's upper mantle to a depth of ~350 km (e.g. Ringwood, 1975; Bass and Anderson, 1984), where it transforms to a high-pressure monoclinic polymorph (e.g. Pacalo and Gasparik, 1990; Kanzaki, 1991). Several mineralogical (e.g.

* E-mail: matteo.alvaro@unipd.it
† Present address: Dipartimento di Scienze della Terra e dell'Ambiente, Università degli Studi di Pavia, Italy
DOI: 10.1180/minmag.2015.079.1.07

Howell *et al*., 2010; Nestola *et al*., 2011; Angel *et al*., 2014*a*,*b*, 2015) and geophysical (e.g. Panning and Romanowicz, 2006; Kustowski *et al*., 2008) investigations have focused on the extremely complex geodynamic processes occurring at that depth. In recent decades, several studies have focused on the behaviour of orthopyroxenes with different compositions under extreme conditions of pressure and temperature and using a wide spread of experimental and computational techniques (e.g. Frisillo and Buljan, 1972; Frisillo and Barsch, 1972; Yang and Ghose, 1994; Hugh-Jones, 1997; Angel and Jackson, 2002; Miyake *et al*., 2004; Nestola *et al*., 2006; Perrillat *et al*., 2007; Gatta *et al*., 2007*a*,*b*). The large number of investigations on orthopyroxene is probably due to the very wide range of geological environments in which this mineral occurs, from magmatic to metamorphic rocks and meteorites, and to the wide range of composition found in nature. Investigation of the elastic properties of host minerals and their inclusions devoted to the determination of the entrapment pressures (P_e) has been demonstrated recently to be an extremely useful tool for understanding mantle-mineral stability fields (Howell *et al*., 2012; Nestola *et al*., 2011; Angel *et al*., 2014*a*,*b*, 2015; Nestola, 2015; Milani *et al*., 2015). However, the use of OPX elastic properties applied to the inclusion-host systems elastic methods requires very accurate and precise knowledge of their thermoelastic behaviour as a function of composition. With regard to the high-temperature behaviour of orthopyroxene, X-ray and neutron diffraction studies (single crystal and powder) on thermoelastic and structural behaviour have been performed on the (Fe,Mg)SiO_3 series to investigate the relationship between Fe-Mg substitution and thermal expansion behaviour (e.g. Frisillo and Barsch, 1972; Yang and Ghose, 1994; Gatta *et al*., 2007*a*,*b*). More recently, the thermal expansion behaviour as a function of more complex compositions (i.e. natural crystals) including Al, Ca, Mg and Fe has been studied at high-*T* and high-*P* conditions (e.g. Nestola *et al*., 2006; Gatta *et al*., 2007*b* and references therein). Among the OPX compositions found in nature, MnMg-pyroxene, isostructural with ortho-enstatite (OEN), was described first by Petersen *et al*. (1984) and referred to historically as donpeacorite in siliceous marble units from Balmat, New York (Brown *et al*., 1980). Moreover, as shown by Stimpfl (2005), Mn-rich Fe-free orthopyroxenes undergo an exchange reaction with increasing temperature similar to that of Fe-Mg OPX already investigated by several authors in the past few decades (e.g. Saxena *et al*. 1989; Ganguly and Domeneghetti, 1996; Domeneghetti *et al*., 1995; Stimpfl *et al*., 1999). Stimpfl (2005) demonstrated clearly that preferential occupancy of the *M*2 site as Mn >> Fe^{2+} > Mg implies that the assignment of Fe^{2+} + Mn = Fe* as one species, typically implemented to determine the quenched-site occupancies in Fe-rich/Mn-poor orthopyroxene, should be abandoned and that Mn should be considered to be completely ordered at *M*2. While it is then clear that Fe-rich and Mn-rich Mg-OPX have different partitioning behaviour, it is not known how the Fe-Mn substitution affects the thermoelastic properties of these mineral phases. Therefore, the aim of this present work was to investigate the high-temperature behaviour of two Mg-OPX with contrasting *M*2 site compositions (Mn-rich, DP N.1 and Fe-rich, B22 N.60) for a closer comparison of their thermal behaviour thus clarifying the effect of Fe-Mg-Mn substitution on the thermoelastic properties of OPX.

Experimental

Samples

Two *Pbca* orthopyroxene single crystals named DP N.1 and B22 N.60 were used for this study. Sample DP N.1 is a donpeacorite crystal [$Mn_{0.54}Ca_{0.03}Mg_{1.43}Si_2O_6$, X_{Mn} = 0.27, size 150 μm × 100 μm × 80 μm] selected from a small sample from Balmat marbles, New York provided by E.U. Petersen (see Petersen *et al*., 1984 for further details). Sample B22 N.60 is a bronzite crystal [$Fe_{0.54}Ca_{0.03}Mg_{1.43}Si_2O_6$; X_{Fe} = 0.27, size 200 μm × 190 μm × 90 μm] picked out from the granulite sample B22, from Wilson Terrane, North Victoria Land, Antarctica, studied previously by Tarantino *et al*. (2002). The two single crystals were selected for high-*T* single-crystal X-ray diffraction (SC-XRD) experiments on the basis of optically sharp extinction and diffraction peak profiles (not more than 0.14º FWHM, Full Width at Half Maximum).

Room-temperature single-crystal X-ray diffraction

The X-ray intensity data of the two selected crystals DP N.1 and B22 N.60 were collected on a three-circle Bruker AXS SMART APEX diffractometer, equipped with a CCD detector (graphite-monochromatized Mo*K*α radiation, λ =

https://doi.org/10.1180/minmag.2015.079.1.07 Published online by Cambridge University Press

0.71073 Å, 40 kV, 30 mA). A 0.3 mm MonoCap collimator was used to collect the data on the crystals. The Bruker *SMART* software (Bruker-AXS ©) package was used. A total of 9000 frames (frame resolution 512 × 512 pixels) were collected with ten different goniometer settings using the ω-scan mode (scan width: 0.2º ω; exposure time: 10–20 s per frame depending on size of the crystals; detector–sample distance: 5.02 cm). About 13,900 reflections were collected for each crystal. A completeness of ~99% on the measured data was achieved up to θ = 55º. The Bruker *SAINT+* software v6.45A (Bruker-AXS ©) was used for data reduction, which included intensity integration, and background and Lorentz-polarization corrections. The semi-empirical absorption correction of Blessing (1995), based on the determination of transmission factors for equivalent reflections, was applied using the program *SADABS* (Sheldrick, 1996). The unit-cell parameters (see Table 1) were obtained by a least-squares procedure that refines the position of ~7000 reflections in the range 6–110º2θ, together with the sample–detector distance and aberration (i.e. X, Y, centre, pitch, roll and yaw). In the same table, the value of the discrepancy factor R_{int} calculated from the average of the $[F_o]^2$ values of equivalent pairs in *mmm* Laue symmetry is also reported. The observed F_o^2 values were then treated with a full-matrix least-squares refinement in the *Pbca* space group using *SHELX-97* (Sheldrick, 2008) starting from the atomic coordinates reported by Stimpfl (2005) for donpeacorite sample DP1 and for sample B22 by Tarantino *et al*. (2002). Individual weights and the weighting scheme suggested by the program were used. The extinction correction was applied with the procedures of program *SHELX-97*.

The atomic scattering curves were taken from the *International Tables for X-ray Crystallography* (Ibers and Hamilton, 1970). Neutral *vs*. ionized scattering factors were refined in all sites that are not involved in chemical substitutions (Hawthorne *et al*., 1995) and complete ionization was assumed for Mg, Fe and Mn in *M*1 and *M*2 sites. Table 1 also reports the mean atomic numbers (m.a.n.) in electrons per formula unit (e.p.f.u.) at the *M*1 and *M*2 sites obtained when the structure refinement reached convergence, without introducing the chemical constraints. The relevant structural information (bond distances and angle, polyhedra volumes and distortions) are reported in Table 2.

Full-matrix least-squares with chemical constraints were then carried out to obtain the site partitioning for both crystals. For the donpeacorite sample, the microprobe analysis by Stimpfl (2005) was adopted while for the bronzite sample that provided by Tarantino *et al*. (2002) for sample B22 was used. The site distribution of *M*1 and *M*2 was obtained as in Domeneghetti *et al*. (2007) but accounting for the stronger preference for the *M*2 site of Mn compared to Fe^{2+} as observed by Stimpfl (2005). The Fe^{2+}/Mg and Mn/Mg order degrees were estimated using the intracrystalline distribution coefficient k_D expressed as: $k_D = X_{Mn}^{M1}[1 - X_{Mn}^{M2}]/ X_{Mn}^{M2}[1 - X_{Mn}^{M1}]$ for donpeacorite where $X_{Mn}^{M1} = (Mn)_{M1}/ (Mn+ Mg)_{M1}$ and $X_{Mn}^{M2} = (Mn)_{M2}/ (Mn+ Mg)_{M2}$ and $k_D = X_{Fe}^{M1}[1- X_{Fe}^{M2}] / X_{Fe}^{M2}[1- X_{Fe}^{M1}]$ for bronzite where $X_{Fe}^{M1} = (Fe)_{M1}/ (Fe + Mg)_{M1}$ and $X_{Fe}^{M2} = (Fe)_{M2}/ (Fe + Mg)_{M2}$. The k_D values are reported in Table 3 together with the site populations for both samples.

The positional and atomic displacement parameters are reported in electronic Tables 4 and 5 and have been deposited with the Principal Editor of *Mineralogical Magazine*. They are available from www.minersoc.org/pages/e_journals/dep_mat_mm.html.

Ex situ annealing experiments

As a consequence of the Mn-Mg and Fe-Mg exchange reactions occurring in orthopyroxenes, the extent of ordering decreases with increasing temperature. However, even though the effect of the disorder taking place during the heating experiment should be negligible (see Tarantino *et al*., 2002), the selected crystals of donpeacorite and bronzite have been annealed previously at high *T* '*ex situ*' and then quenched following the protocol described by Alvaro *et al*. (2011), Pandolfo *et al*. (2015), Alvaro *et al*. (2015) and Domeneghetti *et al*. (2013) in order to prevent any unexpected contribution to the thermal expansion. Therefore, the thermal expansion was measured on the two samples with a disordered distribution of Mn-Mg and Fe-Mg, respectively.

Following the geothermometer calibration given by Stimpfl (2005), the crystal in this study was annealed at 1273 K for 48 h to obtain a fully disordered distribution of Mn-Mg in donpeacorite. The same procedure (i.e. annealing temperature and time) was adopted for the B22 crystal.

After each annealing experiment, intensity data collection and structural refinements were performed on the heat-treated crystals (see

https://doi.org/10.1180/minmag.2015.079.1.07 Published online by Cambridge University Press

TABLE 1*a*. Unit-cell parameters and information on data collection and structure refinement for the donpeacorite crystal (DP N.1): untreated, annealed *ex situ* at 1273 K and after the high-temperature *in situ* experiment.

	Untreated	Annealed for 48 h, 1273 K	After HT *in situ* experiment
a (Å)	18.3550(8)	18.3561(9)	18.3790(2)
b (Å)	8.8789(7)	8.8803(6)	8.8817(10)
c (Å)	5.2359(5)	5.2357(4)	5.2383(6)
V (Å^3)	853.31(11)	853.46(10)	855.06(17)
I_{ind}	2240	2252	2242
R_1	3.87	3.85	4.01
wR_2	8.26	7.72	8.14
S	1.145	1.127	1.135
m.a.n. M1	12.08(6)	13.20(6)	12.77(6)
m.a.n. M2	19.73(8)	18.78(6)	19.21(8)
m.a.n. M1+M2	31.81(10)	31.98(8)	31.98(10)

Note: $R_1 = \Sigma||F_{obs}| - |F_{calc}||/\Sigma|F_{obs}|$; $wR_2 = \{\Sigma[w(F^2_{obs} - F^2_{calc})^2]/\Sigma[w(F^2_{obs})^2]\}^{0.5}$, $w = 1/[\sigma^2(F^2_{obs}) + (0.01{\cdot}P)^2]$, $P = [\mathrm{Max}(F^2_{obs},0) + 2{\cdot}F^2_{calc}]/3$.
m.a.n. = mean atomic number.

TABLE 1*b*. Unit-cell parameters and information on data collection and structure refinement for the bronzite crystal (B22 N.60):untreated, annealed *ex situ* at 1273 K and after the high-temperature *in situ* experiment.

	Untreated	Annealed for 48 h, 1273 K	After HT *in situ* experiment
a (Å)	18.2864(6)	18.2877(6)	18.2843(5)
b (Å)	8.8782(4)	8.8778(4)	8.8763(4)
c (Å)	5.2057(3)	5.2069(3)	5.2070(3)
V (Å^3)	845.15(7)	845.36(7)	845.08(7)
I_{ind}	2245	2238	2246
R_1	2.40	3.28	3.20
wR_2	5.48	7.19	6.90
S	1.084	1.120	1.111
m.a.n. M1	12.39(5)	14.18(7)	13.61(6)
m.a.n. M2	20.01(5)	18.23(7)	18.85(6)
m.a.n. M1+M2	32.40(7)	32.41(10)	32.46(9)

Note: $R_1 = \Sigma||F_{obs}| - |F_{calc}||/\Sigma|F_{obs}|$; $wR_2 = \{\Sigma[w(F^2_{obs} - F^2_{calc})^2]/\Sigma[w(F^2_{obs})^2]\}^{0.5}$, $w = 1/[\sigma^2(F^2_{obs}) + (0.01{\cdot}P)^2]$, $P = [\mathrm{Max}(F^2_{obs},0) + 2{\cdot}F^2_{calc}]/3$.
m.a.n. = mean atomic number.

Tables 2 and 3 and deposited Tables 4 and 5) following the same procedure as reported in the section "Room temperature X-ray diffraction" (see also Fioretti *et al*. 2007; Alvaro *et al*., 2011; Domeneghetti *et al*., 2013; and Alvaro *et al*. 2015 for further details). It is clear that both crystals show a more disordered distribution of Mn-Mg and Fe-Mg, respectively compared to the untreated ones. It is also evident that, at the same *T* and in the same annealing time, bronzite disordered more than donpeacorite as expected by the different partitioning behaviour of Fe compared to Mn (Stimpfl, 2005).

High-temperature single-crystal X-ray diffraction

The high-temperature SC-XRD experiment has been performed on the previously heat-treated crystals DP N.1 and BR N.60 with a Philips

https://doi.org/10.1180/minmag.2015.079.1.07 Published online by Cambridge University Press

TABLE 2. Structure refinement results: bond distances (Å) and angles (º), polyhedra volumes (Å^3) and distortions.

	DP N.1[1]	DP N.1[2]	DP N.1[3]	B22 N.60[1]	B22 N.60[2]	B22 N.60[3]
M1–						
O2A	2.0267	2.0286	2.0294	2.0274	2.0282	2.0283
O1A	2.0424	2.0461	2.0457	2.0279	2.0353	2.0332
O2B	2.0473	2.0504	2.0505	2.0592	2.0609	2.0596
O1B	2.0672	2.0701	2.0697	2.0607	2.069	2.0651
O1A	2.1477	2.1566	2.1542	2.1484	2.1552	2.1526
O1B	2.1796	2.1835	2.1834	2.1684	2.1713	2.1705
V(M1)	11.966(10)	12.032(10)	12.028(13)	11.901(15)	11.977(30)	11.948(41)
Distortion*	0.008	0.0085	0.0081	0.0094	0.0098	0.0096
<M1–O>	2.085	2.089	2.089	2.082	2.087	2.085
M2–						
O2B	2.0418	2.0303	2.0374	1.995	1.9929	1.994
O2A	2.1068	2.0956	2.1014	2.0512	2.049	2.0494
O1B	2.1338	2.1224	2.1278	2.1062	2.0954	2.0991
O1A	2.16	2.1509	2.1563	2.1482	2.1371	2.1409
O3A	2.3275	2.3289	2.3302	2.341	2.3347	2.3359
O3B	2.536	2.5525	2.5489	2.4878	2.486	2.4871
V(M2)	13.374(10)	13.319(10)	13.376(13)	12.939(31)	12.870(46)	12.891(36)
Distortion*	0.0852	0.084	0.0846	0.0778	0.0756	0.0765
<M2–O>	2.218	2.213	2.217	2.187	2.182	2.184
O3A–O3A–O3A	164.01 (0.07)	163.74 (0.07)	163.88 (0.07)	163.38 (0.06)	162.59 (0.07)	162.81 (0.07)
O3B–O3B–O3B	145.55 (0.07)	145.40 (0.07)	145.51 (0.07)	142.09 (0.05)	141.56 (0.07)	141.71 (0.06)
SiA–						
O2A	1.5920(9)	1.5917(8)	1.5921(8)	1.5966(6)	1.5959(8)	1.5955(8)
O1A	1.6115(9)	1.6109(8)	1.6135(9)	1.6108(6)	1.6106(8)	1.6100(8)
O3A	1.6460(9)	1.6438(8)	1.6449(9)	1.6409(6)	1.6403(8)	1.6410(8)
O3A	1.6685(9)	1.6672(8)	1.6689(9)	1.6599(6)	1.6611(8)	1.6605(8)
SiB–						
O2B	1.5943(9)	1.5928(8)	1.5935(9)	1.5982(6)	1.5962(8)	1.5964(8)
O1B	1.6156(9)	1.6166(8)	1.6183(9)	1.6204(6)	1.6201(8)	1.6197(8)
O3B	1.6710(9)	1.6687(8)	1.6697(9)	1.6686(7)	1.6705(8)	1.6696(8)
O3B	1.6752(9)	1.6726(8)	1.6745(9)	1.6738(6)	1.6746(8)	1.6751(8)

Data collected on: [1]Natural sample; [2]Sample annealed at 1273 K for 48 h; [3]Sample after the high-temperature *in situ* experiments.
* Distortion parameters calculated using the *IVTON* program (Balić Žunić and Vicković, 1996).

PW1100 operated with *FEBO* software (control software developed locally) equipped with a micro-furnace controlled by a Eurotherm control unit at the Department of Earth and Environment Sciences, University of Pavia, Italy.

Each crystal was mounted inside quartz vials (0.3 mm inner diameter and 26 mm long) together with a small iron wire to prevent Fe^{2+} oxidation using the same procedure as described by Pandolfo *et al*. (2015) and was held in place by means of quartz wool. The vial was mounted on a metal goniometer head on the diffractometer operating with Mo$K\alpha$ radiation at 30 mA/55 kV and using a 0.5 mm short collimator. The micro-furnace with a H-shaped Pt–Rh resistance heater and a Pt:Pt–Rh thermocouple inside a steel cylindrical cage 2.5 cm wide, closed with a Kapton film, was placed on top of the goniometer head. The device, calibrated before the experiment following the procedure described by Pandolfo *et al*. (2015), allows the collection of diffraction data up to θ_{max} = 34º and T_{max} = 1473 K.

https://doi.org/10.1180/minmag.2015.079.1.07 Published online by Cambridge University Press

TABLE 3*a*. Site populations (in a.p.f.u.) for the donpeacorite crystal (DP N.1): untreated, annealed *ex situ* at 1000ºC and after the high-temperature *in situ* experiment.

Site	Cations	Untreated	Annealed for 48 h, 1273 K	After HT *in situ* experiment
T	Si	1.9973	1.9971	1.9972
	Al	0.0027	0.0029	0.0028
*M*1	Mg	0.9948(18)	0.9169(18)	0.9479(18)
	Fe^{3+}	0.0000	0.0000	0.0000
	Mn	0.0039(18)	0.0817(18)	0.0507(18)
	Cr	0.0000	0.0000	0.0000
	Ti	0.0014	0.0015	0.0014
*M*2	Mg	0.4361(21)	0.5078(20)	0.4764(21)
	Ca	0.0248	0.0249	0.0252
	Mn	0.5391(22)	0.4673(22)	0.4984(22)
	Na	0.0000	0.0000	0.0000
	X^{Mn}M1	0.0039	0.0818	0.0508
	X^{Mn}M2	0.5528	0.4792	0.5113
	k_D	0.0031	0.0968	0.0511
	m.a.n. M1+M2	31.27	31.35	31.35

$k_D = X_{Fe}^{M1}[1 - X_{Fe}^{M2}] / X_{Fe}^{M2}[1 - X_{Fe}^{M1}]$
m.a.n. = mean atomic number.

TABLE 3*b*. Site populations (in a.p.f.u.) for the bronzite crystal (B22 N.60): untreated, annealed *ex situ* at 1000ºC and after the high-temperature *in situ* experiment.

Site	Cations	Untreated	Annealed for 48 h, 1273 K	After HT *in situ* experiment
T	Si	1.9860	1.9855	1.9856
	Al	0.0140	0.0145	0.0145
*M*1	Mg	0.9719(15)	0.8440(18)	0.8850(18)
	Fe^{3+}	0.0000	0.0000	0.0000
	Fe	0.0179(16)	0.1456(20)	0.1045(19)
	Cr	0.0064	0.0065	0.0065
	Ti	0.0038	0.0040	0.0039
*M*2	Mg	0.4148 (18)	0.5428(22)	0.4988(20)
	Ca	0.0239	0.0239	0.0241
	Mn	0.0123	0.0123	0.0127
	Fe	0.5490(24)	0.4210(26)	0.4644(25)
	X^{Fe}(M1)	0.0181	0.1471	0.1056
	X^{Fe}(M2)	0.5696	0.4368	0.4821
	k_D	0.0139	0.2224	0.126
	m.a.n. M1+M2	32.40	32.40	32.44

$k_D = X_{Fe}^{M1}\ [1 - X_{Fe}^{M2}] / X_{Fe}^{M2}\ [1 - X_{Fe}^{M1}]$.
m.a.n. = mean atomic number.

https://doi.org/10.1180/minmag.2015.079.1.07 Published online by Cambridge University Press

TABLE 6*a*. Unit-cell parameters measured by single-crystal X-ray diffraction with increasing temperature for sample DP N.1.

T (K)	*a* (Å)	*b* (Å)	*c* (Å)	*V* (Å^3)
Before HT	18.3550(7)	8.8789(5)	5.2359(4)	853.31(9)
303	18.3561(6)	8.8803(4)	5.2357(3)	853.46(7)
323	18.3587(8)	8.8814(6)	5.2367(4)	853.85(10)
373	18.3647(8)	8.8868(6)	5.2394(4)	855.09(10)
423	18.3726(8)	8.8916(6)	5.2416(3)	856.28(8)
473	18.3788(6)	8.8979(5)	5.2449(3)	857.71(7)
523	18.3868(6)	8.9030(5)	5.2475(3)	859.00(7)
573	18.3938(9)	8.9081(7)	5.2512(4)	860.43(10)
623	18.4015(6)	8.9139(5)	5.2543(3)	861.86(7)
673	18.4118(6)	8.9199(4)	5.2577(3)	863.48(7)
723	18.4202(8)	8.9242(7)	5.2619(3)	864.98(9)
773	18.4312(8)	8.9293(6)	5.2645(4)	866.42(10)
823	18.4373(7)	8.9359(4)	5.2693(3)	868.14(7)
873	18.4495(8)	8.9401(7)	5.2720(4)	869.57(10)
923	18.4576(9)	8.9450(7)	5.2773(5)	871.30(12)
973	18.4672(8)	8.9473(6)	5.2820(4)	872.75(10)
1023	18.4771(8)	8.9507(5)	5.2873(4)	874.43(9)
1073	18.4871(8)	8.9560(6)	5.2901(4)	875.88(10)

Standard deviations are given in parentheses.

TABLE 6*b*. Unit-cell parameters measured by single-crystal X-ray diffraction with increasing temperature for sample bronzite B22 N.60.

T (K)	*a* (Å)	*b* (Å)	*c* (Å)	*V* (Å^3)
Before HT	18.2864(6)	8.8782(4)	5.2057(3)	845.15(7)
303	18.2877(6)	8.8778(4)	5.2069(3)	845.36(7)
323	18.2907(8)	8.8804(6)	5.2078(3)	845.90(8)
373	18.2969(6)	8.8855(4)	5.2097(3)	846.98(7)
423	18.3012(8)	8.8916(5)	5.2133(3)	848.34(8)
473	18.3108(6)	8.8951(4)	5.2152(3)	849.43(7)
523	18.3183(7)	8.9024(5)	5.2183(3)	850.98(8)
573	18.3270(7)	8.9069(5)	5.2215(3)	852.34(8)
623	18.3340(7)	8.9127(6)	5.2246(3)	853.73(8)
673	18.3426(7)	8.9174(5)	5.2284(3)	855.2(8)
723	18.3519(6)	8.9234(4)	5.2308(3)	856.60(7)
773	18.3606(6)	8.9298(4)	5.2344(3)	858.21(7)
823	18.3692(6)	8.9356(5)	5.2381(3)	859.78(7)
873	18.3786(6)	8.9407(5)	5.2419(3)	861.34(7)
923	18.3881(7)	8.9465(5)	5.2457(3)	862.97(8)
973	18.3941(7)	8.9520(4)	5.2501(3)	864.50(7)
1023	18.4040(6)	8.9569(5)	5.2536(3)	866.02(7)
1073	18.4129(7)	8.9624(5)	5.2587(3)	867.81(8)

Standard deviations are given in parentheses.

https://doi.org/10.1180/minmag.2015.079.1.07 Published online by Cambridge University Press

Accurate and precise unit-cell parameters were collected for the sample upon heating from 298 K to 1073 K with steps of 50 K. At each temperature step the unit-cell parameters were calculated by least-squares fitting on a group of 60 selected reflections following the LAT procedure described by Pandolfo *et al*. (2015). The results of the aforementioned procedure for the unit-cell parameter measurements are reported in Table 6 and Fig. 1. Diffraction-peak profiles were collected for each temperature step on the same 60 reflections used for the LAT procedure to

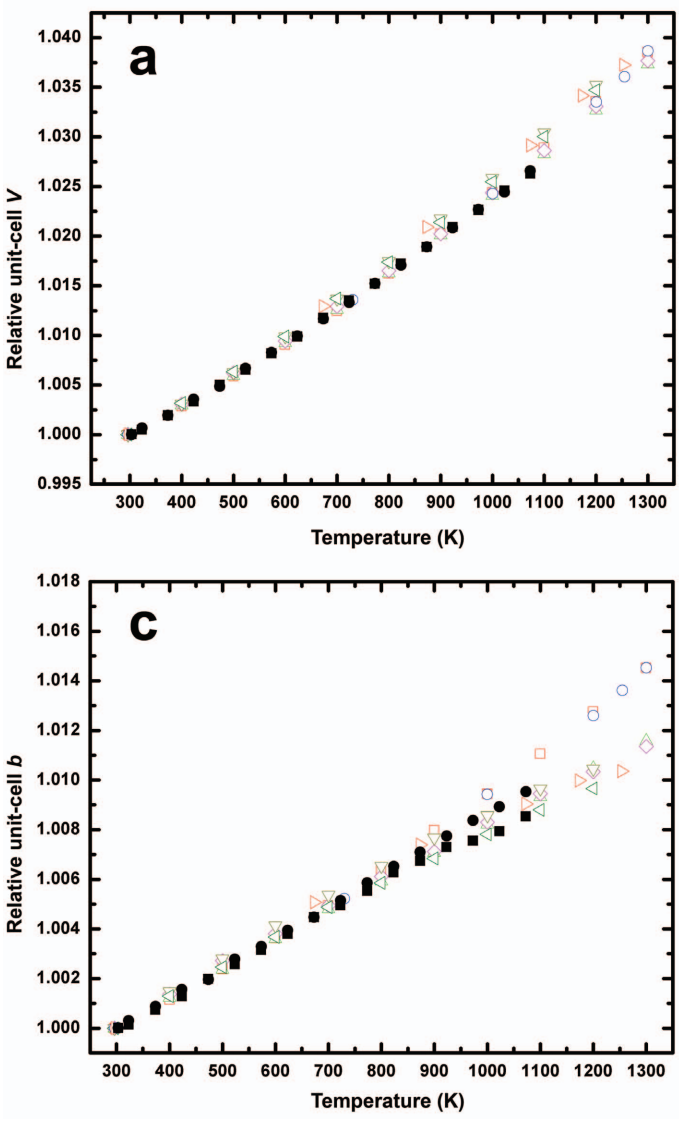

FIG. 1 (*this and facing page*). Relative unit-cell volume (*a*) and lattice parameters (*b*, *c*, *d*) as a function of temperature for all the samples analysed. Filled squares and circles, both fitted with a Fei-EoS (α_2 were constrained and fixed to zero), represent DP N.1 and B22 N.60 samples, respectively. Open symbols represent data from Yang and Ghose (1994): blue circles for Fs_0; red squares for Fs_{20}; green upwards-pointing triangles for Fs_{40}; magenta diamond for Fs_{50}; dark-yellow downwards-pointing triangles for Fs_{75}; olive-green left-pointing triangles for Fs_{83} and orange right-pointing triangles for Fs_{100}.

https://doi.org/10.1180/minmag.2015.079.1.07 Published online by Cambridge University Press

constantly evaluate the quality of the crystal (i.e. FWHM, position, background and the crystal offsets).

To check whether any ordering in Mn/Mg and Fe^{2+}/Mg may have taken place during the high-*T* experiment, further intensity data collections were performed on each of the two recovered crystals DP N.1 and B22 N.60 (following the same procedure as in the "Room-temperature single-crystal X-ray diffraction" section). The results are reported in Tables 1, 2 and 3 for easier comparison with those obtained after the first *ex situ* annealing. On the basis of the results of the structure refinements with chemical constraints and the k_D values, it appears that some ordering occurred for both samples.

Results and discussion

Room-T structure and lattice parameters

In the orthopyroxene structure, the two crystallographically non-equivalent octahedral *M*1 and *M*2 sites (Smyth, 1973; Sueno *et al*., 1976) are mainly occupied by Mg and Fe for bronzite and Mg and

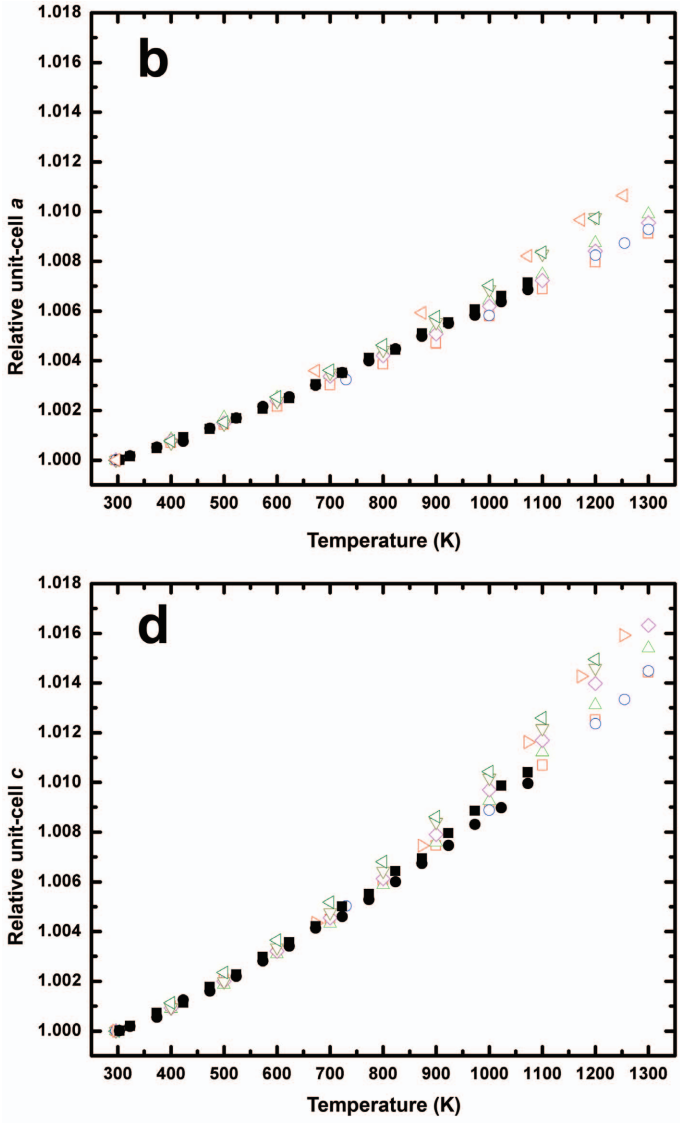

https://doi.org/10.1180/minmag.2015.079.1.07 Published online by Cambridge University Press

Mn for donpeacorite. Both Fe and Mn have a stronger preference for the larger and more distorted *M*2 site (Hugh-Jones, 1997; Domeneghetti and Steffen, 1992; Tarantino *et al*., 2002; Stimpfl, 2005; and references therein). In the natural donpeacorite and bronzite crystals of this study, Mn and Fe are almost totally ordered at site *M*2 (see Table 3) due to the larger Mn (ionic radius = 0.83 Å) compared to Fe (ionic radius = 0.78 Å), the *M*2 site of donpeacorite is significantly larger and more distorted with respect to that of bronzite (see Table 3).

As shown in Table 2, the deformation of the M2 polyhedra decreases with decreasing Mn and Fe contents due to disordering (i.e. from 0.0852 to 0.084 and from 0.0778 to 0.0756 for DP N.1 and B22 N.60, respectively).

The structural changes occurring during the disordering process for the bronzite B22 N.60 sample are in perfect agreement with the observation reported by Domeneghetti *et al*. (1985) for Fe-Mg orthopyroxenes. In particular, the Fe exchange (0.128 atoms per formula unit (a.p.f.u.)) between the *M*2 and *M*1 site causes (1) an increase in the M1 polyhedra volume (by 0.076 $Å^3$) and the relevant bond lengths; (2) a decrease in the M2 polyhedra volume (by 0.069 $Å^3$) and bond lengths which in turns leads to a decrease of the O3–O3–O3 kinking angles (by 0.79º and 0.53º for the A-chain and the B-chain, respectively). Whereas the structural changes occurring during the disordering process at 1273 K for the donpeacorite sample are in perfect agreement with those reported by Stimpfl (2005) on a donpeacorite sample heated at 1253 K.

In this present study of the DP N.1 sample the exchange of 0.0718 a.p.f.u. of Mn between the *M*2 and *M*1 site produces an increase in the polyhedra volume of 0.066 $Å^3$ for the *M*1 site, greater than the decrease (by 0.055 $Å^3$) for the *M*2 site. While for the *M*1 site the increase in the polyhedra volume occurs with the lengthening of all the M1−O bond distances, the smaller decrease in M2 volume occurs mainly because of the pronounced shortening of the M2−O1 and M2−O2 bond distances hampered by the lengthening of the M2−O3 bond distances (mostly the M2−O3B, see Table 2). Such differential shortening is the main cause of the greater distortion of the M2 polyhedron for DP with respect to B22 N.60 that contributes to a smaller decrease of both the A and B tetrahedra chain kinking angles during the disordering process.

Such deformation occurs mainly along [1 0 0] and [0 0 1] directions (i.e. **a** and **c** lattices, respectively). The deformation along [0 0 1] occurs mostly because of the polyhedra volume change that affects the kinking angle by straightening both the TB and TA chains of tetrahedra (see above). Such a change is confirmed by the greater expansion of the **c** lattice parameter for the DP sample (0.6%, ~0.035 Å) which, at room *T*, is longer than that of bronzite B22 orthopyroxene (see Table 2). The deformation of the M2 polyhedron along [1 0 0] clearly affects the length of the *a* unit-cell parameter at room *T*, which is much longer when compared with that of bronzite (0.4%, ~0.07 Å).

On the other hand, the deformation occurring as a function of Mn content along [0 1 0] is nearly negligible as the structural changes (M1−O and M2−O bond lengths) are balanced by the change in the kinking angle of the TA and TB chain of tetrahedra. Therefore, the **b** lattice parameter is smaller for DP N.1 (Mn opx) than that of the equivalent orthopyroxene on the Fe−Mg series. The structural and the lattice parameters (mostly **a** and **c**) changes at room *T* are probably responsible for the differences in the room-*T* unit-cell volume as a function of composition (see Fig. 2 and Table 2). In Fig. 2, the unit-cell volume obtained on the samples in this present study are plotted together with all the available literature data for pure Fe-Mg synthetic orthopyroxenes by Yang and Ghose (1994) against the Fe/(Fe+Mg) and Mn/(Mn+Mg) ratio for Fe-Mg orthopyroxene and donpeacorite, respectively. The relationship between Fe-Mg substitution (i.e. Fe/Fe+Mg) and unit-cell volume at room *P*,*T* is not valid for Fe-poor orthopyroxenes (see Fig. 2). In fact, the 8.1 $Å^3$ (~1%) larger room-*T* unit-cell volume of DP N.1 [853.46(7) $Å^3$] compared to that of B22 N.60 [845.36(7) $Å^3$] reflects the larger ionic radius of Mn compared to Fe^{2+}. No further clear trend was found for any of the other room-*T* lattice parameters as a function of composition (see Table 6 and Fig. 2).

Unit-cell parameters evolution with T

As shown in Fig. 1, the normalized unit-cell volume and lattice parameters increase almost linearly with temperature (*T*) for both the completely disordered donpeacorite (DP N.1) and B22 (B22 N.60) samples. Between the two samples there is no difference in the unit-cell volume expansion as a function of temperature.

https://doi.org/10.1180/minmag.2015.079.1.07 Published online by Cambridge University Press

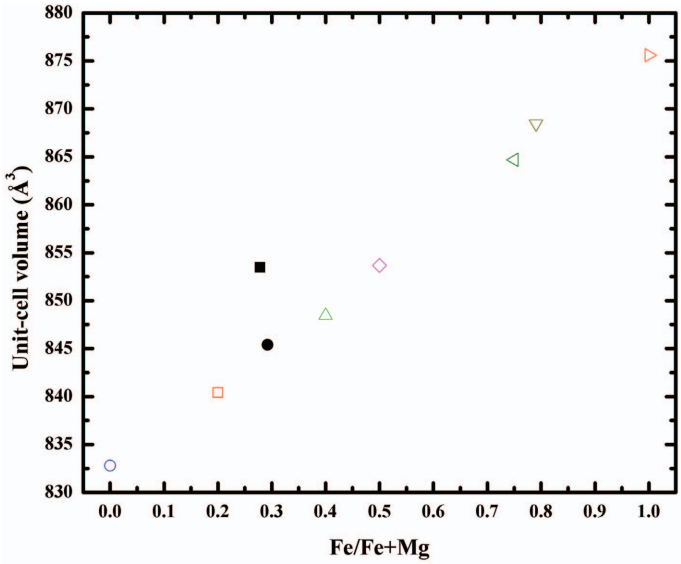

FIG. 2. Unit-cell volume as a function of Fe/(Fe+Mg) values for bronzite samples while Mn/(Mn+Mg) values were considered for the donpeacorite sample. Open symbols represent data for a synthetic sample from Yang and Ghose (1994); filled circles and filled squares are B22 N.60 and DP N.1, respectively.

However, such a volume behaviour is the result of different unit-cell parameter expansion schemes (i.e. the effect of differential thermal expansion behaviour along unit-cell directions). Over the entire T range investigated, the **b** lattice for DP N.1 shows a much smaller expansion (0.84%) than that of B22 N.60 (0.94%). Such a difference occurs mostly at a T >800 K. On the other hand, in the investigated T range, **a** and **c** lattice parameters for DP N.1 show larger expansion (0.71% and 1.03% for a and c, respectively) than that of B22 N.60 (0.68% and 0.98% for **a** and **c**, respectively).

In Fig. 3, the lattice parameters for the samples studied in this work are plotted together with those obtained by SC-XRD on the pure synthetic Fe-Mg orthopyroxenes by Yang and Ghose (1994). B22 N.60 lattice parameters behave as a function of temperature as expected for an intermediate composition (i.e. Fs_{20} and Fs_{40}), whereas the behaviour of DP N.1 is much closer to that of the Fs_{50} because of the Mn presence. Therefore, it seems that the Fe-Mn substitution controls the unit-cell volume expansion with T only by affecting the V_0 unit-cell volume at room T (see Fig. 3).

Unit-cell parameters thermal expansion

For the purpose of comparison all the unit-cell and volume thermal expansion values of both samples were fitted to a Berman-type (Berman, 1988) and Fei-type (Fei, 1995) Equation of State (EoS) using the *Eosfit7c* program (Angel *et al*., 2014*a*). In Table 7, all the fitting results obtained on the samples studied in this present work are shown together with those published and re-calculated for available datasets in the literature (Yang and Ghose, 1994). In order to compare the results from this present study with those re-calculated from the literature, the most reasonable fitting model was that obtained with the Fei-type EoS constraining the α_2 to 0 as those obtained refining the α_2 coefficient led to 'non-physical' results for the lattice parameter thermal expansion coefficients (see Angel *et al*., 2014*a* for further details). Moreover, the results obtained with the Berman-type EoS produced no improvement in the statistical parameters, such as, for instance, the χ^2 values (see Pandolfo *et al*., 2015 for further details). A higher order of the polynomial is not recommended, mainly because of the restricted range of T investigated and/or the small number of data points in the T interval.

At room temperature the relative magnitudes of unit-cell thermal expansion coefficients for both samples in this present study are in the order $\alpha_b > \alpha_c > \alpha_a$, in good agreement with the available literature data for Fe-Mg opx. However, subtle

https://doi.org/10.1180/minmag.2015.079.1.07 Published online by Cambridge University Press

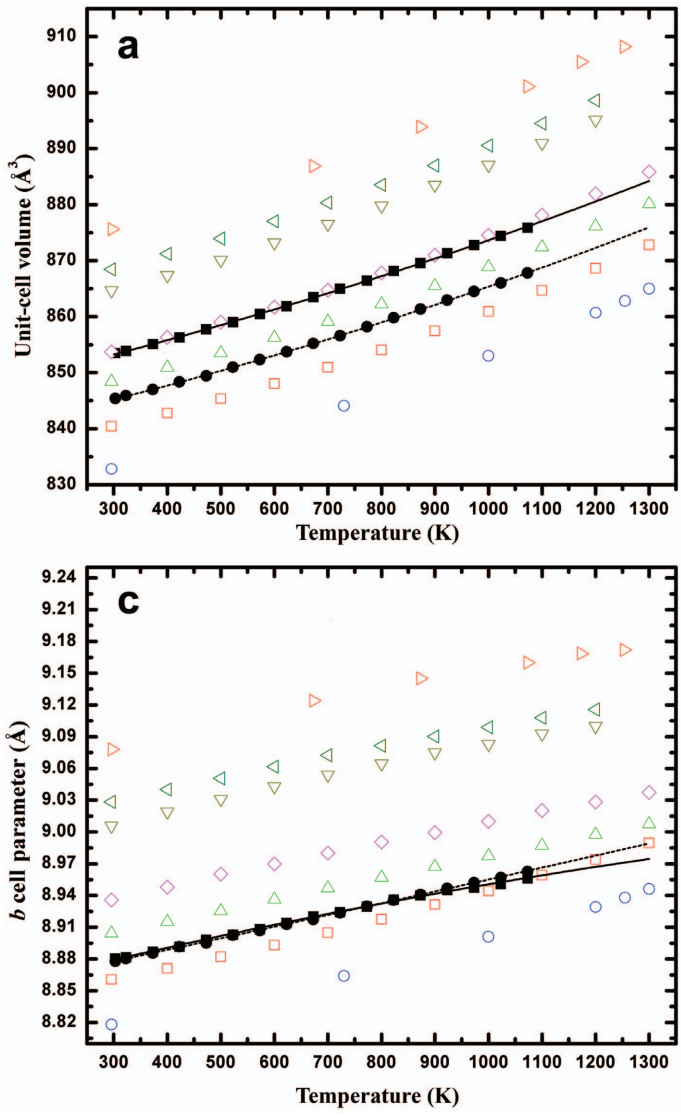

FIG. 3 (*this and facing page*). Unit-cell (*b*,*c*,*d*) and volume (*a*) parameters as a function of temperature for all the samples analysed. Filled squares and circles both fitted with a Fei-EoS (α_2 were constrained and fixed to zero), represent DP N.1 and B22 N.60 samples, respectively. Open symbols represent data from Yang and Ghose (1994): blue circles for Fs_0; red squares for Fs_{20}; green upwards-pointing triangles for Fs_{40}; magenta diamonds for Fs_{50}; dark-yellow downwards-pointing triangles for Fs_{75}; olive-green left-pointing triangles for Fs_{83} and orange right-pointing triangles for Fs_{100}.

differences in the axial thermal expansion between the two samples are evident. The **c** lattice thermal expansion for both samples are nearly identical. On the other hand, the **a** lattice thermal expansion for DP N.1 is smaller than that of B22 N.60 ($\Delta\alpha_a = 0.07 \times 10^{-5}K^{-1}$, see Table 7). Such a difference is compensated by a greater expansion of the **b** lattice for DP N.1 compared to B22 N.60, producing, therefore, a volume thermal expansion difference of only $0.05 \times 10^{-5}K^{-1}$ (with DP N.1 being greater than B22 N.60, although such a difference is smaller than 1 e.s.d. (estimated standard deviation),

https://doi.org/10.1180/minmag.2015.079.1.07 Published online by Cambridge University Press

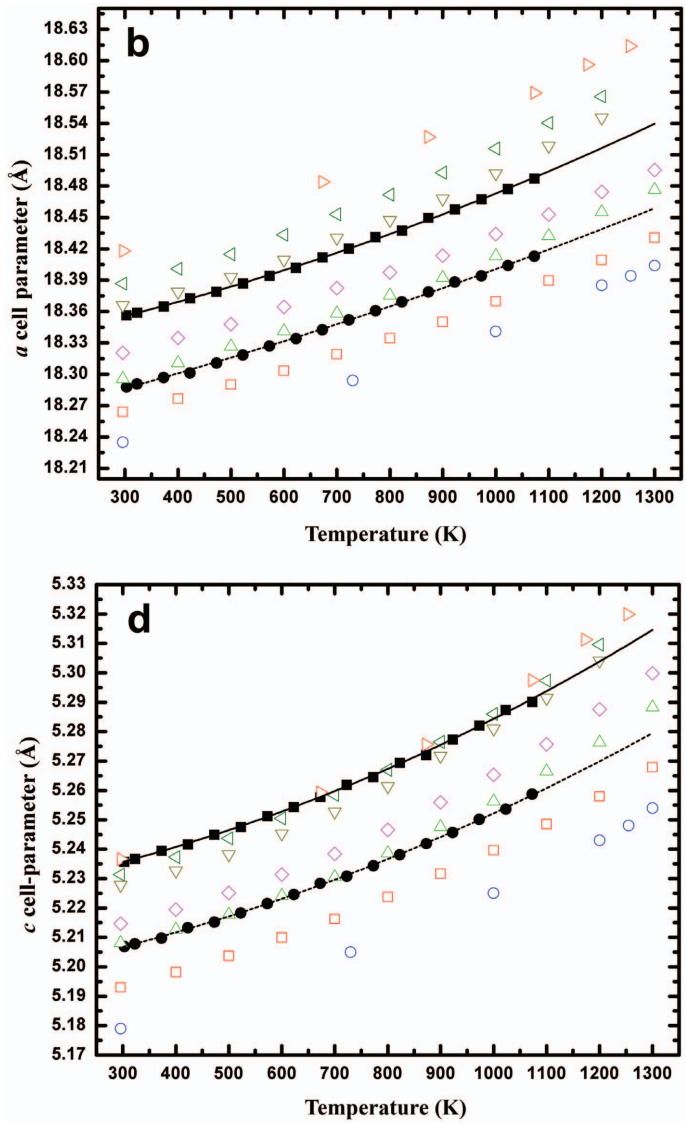

see Table 7). It is clear therefore that, within the e.s.d., the room-T thermal expansion coefficient is not affected by Fe-Mn substitution. At high T, changes in the thermal expansion scheme were observed for all the lattice parameters in both samples ($\alpha_c > \alpha_b > \alpha_a$ for B22 N.60 and $\alpha_c > \alpha_b \geqslant \alpha_a$ for donpeacorite) demonstrating that at high T the two samples show different behaviour mainly because of the changes in the expansion mechanism.

At 1000 K the relationship between the lattice expansion of DP N.1 and B22 N.60 are completely changed with respect to that at 303 K, being $\alpha_{V(DP)} < \alpha_{V(B22)}$, $\alpha_{a(DP)} > \alpha_{a(B22)}$, $\alpha_{b(DP)} < \alpha_{b(B22)}$, $\alpha_{c(DP)} > \alpha_{c(B22)}$.

The negligible effect of the Fe-Mn substitution on the bulk thermal expansion finds its application when dealing with geothermobarometry based on the elastic host-inclusion approach (e.g. Nestola *et al.*, 2011; Howell *et al.*, 2010; Angel *et al.*, 2014*a*,*b*, 2015). In fact, though the compressibility effect is still not known, the nearly identical thermal expansion coefficients will not affect the entrapment pressure (P_e). However, in future

https://doi.org/10.1180/minmag.2015.079.1.07 Published online by Cambridge University Press

TABLE 7*a*. Volume thermal expansion fitting results for the samples in the present study together with those recalculated from the available literature data.

	Fei-type EoS			Fei-type EoS (with $\alpha_2 = 0$)			Berman-type EoS		
	$\alpha_{V,303}$ ($\times 10^{-5}K^{-1}$)	V_0 (Å^3)	χ^2	$\alpha_{V,303}$ ($\times 10^{-5}K^{-1}$)	V_0 (Å^3)	χ^2	$\alpha_{V,303}$ ($\times 10^{-5}K^{-1}$)	V_0 (Å^3)	χ^2
DP N.1	2.31(24)	853.35(4)	0.77	2.94(8)	853.34(6)	2.74	2.93(5)	853.34(6)	2.66
B22 N.60	2.51(25)	845.40(6)	0.93	2.89(7)	845.29(5)	1.52	2.88(4)	845.30(5)	1.47
Fs_0	2.77(24.36)	832.96(4.28)	0.00	2.62(3.11)	832.96(3.79)	0.00	2.60(2.04)	832.96(3.83)	0.00
Fs_{20}	2.64(36)	840.58(14)	0.04	2.64(10)	840.58(10)	0.03	2.62(6)	840.59(10)	0.04
Fs_{40}	2.71(30)	848.61(10)	0.04	2.75(8)	848.60(7)	0.04	2.74(5)	848.61(7)	0.04
Fs_{50}	–	–	0.10	2.83(8)	853.89(7)	0.20	2.82(5)	853.89(7)	0.24
Fs_{75}	2.76(42)	864.86(11)	0.30	2.97(11)	864.82(8)	0.41	2.95(7)	864.83(8)	0.38
Fs_{83}	3.04(40)	868.60(15)	0.35	2.98(10)	868.61(11)	0.31	2.96(7)	868.62(11)	0.33
Fs_{100}	2.67(178)	875.74(47)	9.10	3.18(27)	875.72(37)	6.74	3.17(18)	875.73(37)	6.61

Data for samples Fs_0, Fs_{20}, Fs_{40}, Fs_{50}, Fs_{75}, Fs_{83} and Fs_{100} are taken from Yang and Ghose (1994).
– Indicates that the results obtained from the fitting lead to non-physical α values (see Angel *et al*., 2014*b* for further details).

TABLE 7*b*. Lattice parameter, **a**, thermal expansion fitting results for the samples in the present study together with those recalculated from the available literature data.

	Fei-type EoS			Fei-type EoS (with $\alpha_2 = 0$)			Berman-type EoS		
	$\alpha_{a,303}$ ($\times 10^{-5}K^{-1}$)	a_0 (Å)	χ^2	$\alpha_{a,303}$ ($\times 10^{-5}K^{-1}$)	a_0 (Å)	χ^2	$\alpha_{a,303}$ ($\times 10^{-5}K^{-1}$)	a_0 (Å)	χ^2
DP N.1	0.59(13)	18.3562(5)	1.54	0.71(3)	18.3551(5)	1.85	0.70(2)	18.3552(5)	1.81
B22 N.60	0.49(13)	18.2877(6)	1.51	0.77(4)	18.2866(7)	3.23	0.77(2)	18.2859(7)	3.20
Fs_0	0.6(12.4)	18.24(3)	0.00	0.6(9)	18.24(3)	0.00	0.6(6)	18.24(3)	0.00
Fs_{20}	0.67(24)	18.2649(22)	0.10	0.62(7)	18.2652(16)	0.10	0.61(4)	18.2647(17)	0.10
Fs_{40}	–	–	–	–	18.2971(11)	0.18	–	18.2971(11)	0.19
Fs_{50}	0.70(23)	18.3213(20)	0.29	0.71(7)	18.3213(14)	0.26	0.71(4)	18.3206(14)	0.26
Fs_{75}	0.64(26)	18.3668(15)	0.43	0.64(7)	18.3668(11)	0.37	0.64(4)	18.3668(12)	0.38
Fs_{83}	0.67(25)	18.3875(20)	0.11	0.73(7)	18.3872(15)	0.12	0.72(4)	18.3873(15)	0.11
Fs_{100}	0.81(46)	18.4188(38)	3.43	0.87(8)	18.4186(28)	2.33	0.87(6)	18.4187(28)	2.32

Data for samples Fs_0, Fs_{20}, Fs_{40}, Fs_{50}, Fs_{75}, Fs_{83} and Fs_{100} are taken from Yang and Ghose (1994).
– Indicates that the results obtained from the fitting lead to non-physical α values (see Angel *et al*., 2014*b* for further details).

https://doi.org/10.1180/minmag.2015.079.1.07 Published online by Cambridge University Press

TABLE 7*c*. Lattice parameter, **b**, thermal expansion fitting results for the samples in the present study together with those recalculated from the available literature data.

	Fei-type EoS			Fei-type EoS (with $\alpha_2 = 0$)			Berman-type EoS		
	$\alpha_{b,303}$ ($\times 10^{-5}K^{-1}$)	b_0 (Å)	χ^2	$\alpha_{b,303}$ ($\times 10^{-5}K^{-1}$)	b_0 (Å^3)	χ^2	$\alpha_{b,303}$ ($\times 10^{-5}K^{-1}$)	b_0 (Å)	χ^2
DP N.1	0.89(23)	8.8799(4)	1.66	1.32(7)	8.8792(5)	3.62	1.32(4)	8.8792(5)	3.67
B22 N.60	1.10(19)	8.8781(4)	1.70	1.22(5)	8.8773(4)	1.75	1.22(3)	8.8778(4)	1.75
Fs_0	0.82(9.67)	8.819(12)	0.00	1.04(92)	8.8186(96)	0.00	1.03(59)	8.8186(97)	0.00
Fs_{20}	1.06(24)	8.8616(9)	0.07	1.10(7)	8.8615(7)	0.07	1.09(4)	8.8615(7)	0.06
Fs_{40}	1.14(20)	8.905(6)	0.11	1.19(5)	8.9049(5)	0.13	1.19(3)	8.9049(5)	0.13
Fs_{50}	1.46(20)	8.936(8)	0.50	1.28(6)	8.9372(6)	0.68	1.28(4)	8.9372(6)	0.67
Fs_{75}	1.43(24)	9.0067(6)	0.31	1.45(6)	9.0067(5)	0.27	1.46(4)	9.0066(5)	0.28
Fs_{83}	1.29(22)	9.0291(8)	0.24	1.27(6)	9.0292(6)	0.21	1.28(4)	9.0286(7)	0.20
Fs_{100}	1.54(6)	9.0787(11)	1.21	1.53(8)	9.0787(10)	1.18	1.54(6)	9.0787(11)	1.21

Data for samples Fs_0, Fs_{20}, Fs_{40}, Fs_{50}, Fs_{75}, Fs_{83} and Fs_{100} are taken from Yang and Ghose (1994).

Table 7*d*. Lattice parameter, **c**, thermal expansion fitting results for the samples in the present study together with those recalculated from the available literature data.

	Fei-type EoS			Fei-type EoS (with $\alpha_2 = 0$)			Berman-type EoS		
	$\alpha_{c,303}$ ($\times 10^{-5}K^{-1}$)	c_0 (Å)	χ^2	$\alpha_{c,303}$ ($\times 10^{-5}K^{-1}$)	c_0 (Å^3)	χ^2	$\alpha_{c,303}$ ($\times 10^{-5}K^{-1}$)	c_0 (Å)	χ^2
DP N.1	0.85(28)	5.2356(3)	2.15	0.92(6)	5.2357(3)	2.04	0.91(3)	5.2357(3)	2.03
B22 N.60	0.93(20)	5.2068(3)	1.43	0.90(4)	5.2068(2)	1.34	0.90(3)	5.2068(2)	1.38
Fs_0	–	–	–	0.95(1.43)	5.1791(98)	–	0.94(92)	5.1794(97)	–
Fs_{20}	0.91(23)	5.1933(5)	0.04	0.92(6)	5.1933(4)	0.04	0.90(4)	5.1931(4)	0.04
Fs_{40}	0.71(20)	5.2084(4)	0.27	0.80(6)	5.2082(3)	0.34	0.78(4)	5.2081(3)	0.28
Fs_{50}	0.81(19)	5.215(5)	0.10	0.82(6)	5.215(3)	0.09	0.81(4)	5.215(3)	0.10
Fs_{75}	0.72(24)	5.2281(4)	0.58	0.87(7)	5.2279(3)	0.72	0.86(4)	5.2279(3)	0.65
Fs_{83}	1.08(23)	5.2318(5)	0.41	0.98(6)	5.2319(4)	0.41	0.97(4)	5.2319(4)	0.48
Fs_{100}	–	–	–	0.79(15)	5.2369(11)	8.50	0.76(10)	5.2368(11)	8.58

Data for samples Fs_0, Fs_{20}, Fs_{40}, Fs_{50}, Fs_{75}, Fs_{83} and Fs_{100} are taken from Yang and Ghose (1994).
– Indicates that the results obtained from the fitting lead to non-physical α values (see Angel *et al*., 2014*b* for further details).

work, the different axial expansion scheme, due to Fe-Mn substitution, may suggest the possibility that the elastic anisotropy should be accounted for.

Acknowledgements

This work was supported by the ERC starting grant #307322 to F. Nestola.

References

Alvaro, M., Cámara, F., Domeneghetti, M., Nestola, F. and Tazzoli, V. (2011) H*T* $P2_1/c-C2/c$ phase transition and kinetics of Fe^{2+}-Mg order-disorder of an Fe-poor pigeonite: implications for the cooling history of ureilites. *Contributions to Mineralogy and Petrology*, **162**, 599–613.

Alvaro, M., Domeneghetti, M.C., Fioretti, A.M., Cámara, F. and Marinangeli, L. (2015) A new calibration to determine the closure temperatures of Fe-Mg ordering in augite from nakhlites. *Meteoritics & Planetary Science*, DOI: 10.1111/maps.12436.

Angel, R.J. and Jackson, J.M. (2002) Elasticity and equation of state of orthoenstatite, $MgSiO_3$. *American Mineralogist*, **87**, 558–561.

Angel, R.J., Gonzalez-Platas, J. and Alvaro, M. (2014*a*) EosFit7c and a Fortran module (library) for equation

https://doi.org/10.1180/minmag.2015.079.1.07 Published online by Cambridge University Press

of state calculations. *Zeitschrift für Kristallographie*, **229**, 405–419.

Angel, R.J., Mazzucchelli, M.L., Alvaro, M., Nimis, P. and Nestola, F. (2014*b*) Geobarometry from host-inclusion systems: the role of elastic relaxation. *American Mineralogist*, **99**, 2146–2149.

Angel, R.J., Alvaro, M., Nestola, F. and Mazzucchelli, M.L. (2015) Diamond thermoelastic properties and implications for determining the pressure of formation of diamond inclusion systems. *Russian Geology and Geophysics Journal*, **56**, 211–220.

Balić Žunić, T. and Vicković, I. (1996) *IVTON* – a program for the calculation of geometrical aspects of crystal structures and some crystal chemical applications. *Journal of Applied Crystallography*, **29**, 305–306.

Bass, J.D. and Anderson, D.L. (1984) Composition of the upper mantle: Geophysical tests of two petrological models. *Geophysical Research Letters*, **11**, 229–232.

Berman, R.G. (1988) Internally-consistent thermodynamic data for minerals in the system Na_2O–K_2O–CaO–MgO–FeO—Fe_2O_3–Al_2O_3–SiO_2–TiO_2–H_2O–CO_2. *Journal of Petrology*, **29**, 445–522.

Blessing, R.H. (1995) An empirical correction for absorption anisotropy. *Acta Crystallographica Section A*, **51**, 33–38.

Brown, P.E., Essene, E.J. and Peacor, D.R. (1980) Phase relations inferred from field data for Mn pyroxenes and pyroxenoids. *Contributions to Mineralogy and Petrology*, **74**, 417–425.

Domeneghetti, M.C. and Steffen, G. (1992) M1, M2 site populations and distortion parameters in synthetic Mg-Fe orthopyroxenes from Mössbauer spectra and X-ray structure refinements. *Physics and Chemistry of Minerals*, **19**, 298–306.

Domeneghetti, M.C., Molin, G.M. and Tazzoli, V. (1985) Crystal-chemical implications of the Mg^{2+}-Fe^{2+} distribution in orthopyroxenes. *American Mineralogist*, **70**, 987–995.

Domeneghetti, M.C., Molin, G.M. and Tazzoli, V. (1995) A crystal-chemical model for *Pbca* orthopyroxene. *American Mineralogist*, **80**, 253–267.

Domeneghetti, M.C., Fioretti, A.M., Cámara, F., Molin, G. and Tazzoli, V. (2007) Thermal history of ALH 84001 meteorite by Fe^{2+}-Mg ordering in orthopyroxene. *Meteoritics & Planetary Science*, **42**, 1703–1710.

Domeneghetti, M., Fioretti, A., Cámara, F., McCammon, C. and Alvaro, M. (2013) Thermal history of nakhlites: A comparison between MIL 03346 and its terrestrial analogue Theo's flow. *Geochimica et Cosmochimica Acta*, **121**, 571–581.

Fei, Y. (1995) Thermal expansion. Pp. 29–44 in: *Mineral Physics and Crystallography: a Handbook of Physical Constants* (T.J. Ahrens, editor). AGU Reference Shelf, **Vol. 2**. American Geophysical Union, Washington, DC.

Fioretti, A.M., Domeneghetti, M.C., Molin, G., Cámara, F., Alvaro, M. and Agostini, L. (2007) Reclassification and thermal history of Trenzano chondrite. *Meteoritics & Planetary Science*, **42**, 2055–2066.

Frisillo, A.L. and Barsch, G.R. (1972) Measurement of single-crystal elastic constants of bronzite as a function of pressure and temperature. *Journal of Geophysical Research*, **77**, 6360–6384.

Frisillo, A.L. and Buljan, S.T. (1972) Linear thermal expansion coefficients of orthopyroxene to 1000ºC. *Journal of Geophysical Research*, **77**, 7115–7117.

Ganguly, J. and Domeneghetti, M.C. (1996) Cation ordering of orthopyroxenes from the Skaergaard Intrusion: implications for the subsolidus cooling rates and permeabilities. *Contributions to Mineralogy and Petrology*, **122**, 359–367.

Gatta, G., Rinaldi, R., Knight, K., Molin, G. and Artioli, G. (2007*a*) In-situ high-temperature thermo-elastic behavior and structural response of a mantle orthopyroxene by neutron powder diffraction up to 1200ºC. *Proceedings of the VI Congress of the "Federazione Italiana di Scienze della Terra" (F.I.S.T) – Rimini (Italy), 12–14 September 2007.*

Gatta, G.D., Rinaldi, R., Knight, K., Molin, G. and Artioli, G. (2007*b*) High temperature structural and thermoelastic behaviour of mantle orthopyroxene: an *in situ* neutron powder diffraction study. *Physics and Chemistry of Minerals*, **34**, 185–200.

Hawthorne, F.C., Ungaretti, L. and Oberti, R. (1995) Site populations in minerals; terminology and presentation of results of crystal-structure refinement. *The Canadian Mineralogist*, **33**, 907–911.

Howell, D., Wood, I.G., Dobson, D.P., Jones, A.P., Nasdala, L. and Harris, J.W. (2010) Quantifying strain birefringence halos around inclusions in diamond. *Contributions to Mineralogy and Petrology*, **160**, 705–717.

Howell, D., Wood, I.G., Nestola, F., Nimis, P. and Nasdala, L. (2012) Inclusions under remnant pressure in diamond: a multi-technique approach. *European Journal of Mineralogy*, **24**, 563–573.

Hugh-Jones, D. (1997) Thermal expansion of $MgSiO_3$ and $FeSiO_3$ ortho- and clinopyroxenes. *American Mineralogist*, **82**, 689–696.

Ibers, J. and Hamilton, W. (1970) *International Tables for X-ray Crystallography*. Kynoch Press, Birmingham, UK [pp. 99–101].

Kanzaki, M. (1991) Stability of hydrous magnesium silicates in the mantle transition zone. *Physics of the Earth and Planetary Interiors*, **66**, 307–312.

Kustowski, B., Ekström, G. and Dziewoński, A. (2008) Anisotropic shear–wave velocity structure of the Earth's mantle: A global model. *Journal of*

https://doi.org/10.1180/minmag.2015.079.1.07 Published online by Cambridge University Press

Geophysical Research: Solid Earth (1978–2012), DOI: 10.1029/2007JB005169.

Milani, S., Nestola, F., Alvaro, M., Pasqual, D., Mazzucchelli, M.L., Domeneghetti, M.C. and Geiger, C.A. (2015) Diamond-garnet barometry: The role of garnet compressibility and expansivity. *Lithos*, DOI: 10.1016/j.lithos.2015.03.017.

Miyake, A., Shimobayashi, N. and Kitamura, M. (2004) Isosymmetric structural phase transition of orthoenstatite: Molecular dynamics simulation. *American Mineralogist*, **89**, 1667–1672.

Nestola, F. (2015) The crucial role of crystallography in diamond research. *Rendiconti Lincei*, DOI: 10.1007/s12210-015-0398-1.

Nestola, F., Gatta, G.D. and Ballaran, T.B. (2006) The effect of Ca substitution on the elastic and structural behavior of orthoenstatite. *American Mineralogist*, **91**, 809–815.

Nestola, F., Nimis, P., Ziberna, L., Longo, M., Marzoli, A., Harris, J.W., Manghnani, M.H. and Fedortchouk, Y. (2011) First crystal-structure determination of olivine in diamond: Composition and implications for provenance in the Earth's mantle. *Earth and Planetary Science Letters*, **305**, 249–255.

Pacalo, R. and Gasparik, T. (1990) Reversals of the orthoenstatite–clinoenstatite transition at high pressures and high temperatures. *Journal of Geophysical Research: Solid Earth (1978–2012)*, **95**, 15853–15858.

Pandolfo, F., Cámara, F., Domeneghetti, M.C., Alvaro, M., Nestola, F., Karato, S.-I. and Amulele, G. (2015) Volume thermal expansion along the jadeite-diopside join. *Physics and Chemistry of Minerals*, **42**, 1–14.

Panning, M. and Romanowicz, B. (2006) A three-dimensional radially anisotropic model of shear velocity in the whole mantle. *Geophysical Journal International*, **167**, 361–379.

Perrillat, J.-P., Nestola, F., Sinogeikin, S.V. and Bass, J.D. (2007) Single-crystal elastic properties of $Ca_{0.07}Mg_{1.93}Si_2O_6$ orthopyroxene. *American Mineralogist*, **92**, 109–113.

Petersen, E.U., Anovitz, L.M. and Essene, E.J. (1984) Donpeacorite, $(Mn,Mg)MgSi_2O_6$, a new orthopyroxene and its proposed phase relations in the system $MnSiO_3$–$MgSiO_3$–$FeSiO_3$. *American Mineralogist*, **69**, 472–480.

Ringwood, A.E. (1975) *Composition and Petrology of the Earth's Mantle*. McGraw-Hill, New York.

Saxena, S.K., Domeneghetti, M.C., Molin, G.M. and Tazzoli, V. (1989) X-ray diffraction study of Fe^{2+}-Mg order-disorder in orthopyroxene. Some kinetic results. *Physics and Chemistry of Minerals*, **16**, 421–427.

Sheldrick, G.M. (1996) *SADABS*. University of Göttingen, Germany.

Sheldrick, G.M. (2008) A short history of SHELX. *Acta Crystallographica Section A*, **64**, 112–122.

Smyth, J. (1973) Orthopyroxene structure up to 850ºC. *American Mineralogist*, **58**, 636–648.

Stimpfl, M. (2005) The Mn, Mg-intracrystalline exchange reaction in donpeacorite ($Mn_{0.54}Ca_{0.03}Mg_{1.43}Si_2O_6$) and its relation to the fractionation behavior of Mn in Fe,Mg-orthopyroxene. *American Mineralogist*, **90**, 155–161.

Stimpfl, M., Ganguly, J. and Molin, G. (1999) Fe^{2+}-Mg order-disorder in orthopyroxene: equilibrium fractionation between the octahedral sites and thermodynamic analysis. *Contributions to Mineralogy and Petrology*, **136**, 297–309.

Sueno, S., Cameron, M. and Prewitt, C. (1976) Orthoferrosilite: high-temperature crystal chemistry. *American Mineralogist*, **61**, 38–53.

Tarantino, S.C., Domeneghetti, M.C., Carpenter, M.A., Shaw, C.J.S. and Tazzoli, V. (2002) Mixing properties of the enstatite-ferrosilite solid solution: I. A macroscopic perspective. *European Journal of Mineralogy*, **14**, 525.

Yang, H. and Ghose, S. (1994) Thermal expansion, Debye temperature and Grüneisen parameter of synthetic $(Fe,Mg)SiO_3$ orthopyroxenes. *Physics and Chemistry of Minerals*, **20**, 575–586.

https://doi.org/10.1180/minmag.2015.079.1.07 Published online by Cambridge University Press